

Net on-chip Brillouin gain based on suspended silicon nanowires

This content has been downloaded from IOPscience. Please scroll down to see the full text.

2015 New J. Phys. 17 115005

(<http://iopscience.iop.org/1367-2630/17/11/115005>)

View [the table of contents for this issue](#), or go to the [journal homepage](#) for more

Download details:

IP Address: 157.193.173.51

This content was downloaded on 04/11/2015 at 08:18

Please note that [terms and conditions apply](#).



PAPER

Net on-chip Brillouin gain based on suspended silicon nanowires

OPEN ACCESS

RECEIVED
25 August 2015REVISED
23 September 2015ACCEPTED FOR PUBLICATION
6 October 2015PUBLISHED
3 November 2015

Content from this work
may be used under the
terms of the [Creative
Commons Attribution 3.0
licence](#).

Any further distribution of
this work must maintain
attribution to the
author(s) and the title of
the work, journal citation
and DOI.

Raphaël Van Laer¹, Alexandre Bazin¹, Bart Kuyken, Roel Baets and Dries Van ThourhoutPhotonics Research Group, Ghent University-imec, Belgium
Center for Nano- and Biophotonics, Ghent University, Belgium¹ These authors contributed equally to this work.E-mail: raphael.vanlaer@intec.ugent.be and alexandre.bazin@intec.ugent.be**Keywords:** photon–phonon coupling, silicon photonics, nonlinear optics, Brillouin scattering, optomechanics**Abstract**

The century-old study of photon–phonon coupling has seen a remarkable revival in the past decade. Driven by early observations of dynamical back-action, the field progressed to ground-state cooling and the counting of individual phonons. A recent branch investigates the potential of traveling-wave, optically broadband photon–phonon interaction in silicon circuits. Here, we report continuous-wave Brillouin gain exceeding the optical losses in a series of suspended silicon beams, a step towards selective on-chip amplifiers. We obtain efficiencies up to $10^4 \text{ W}^{-1} \text{ m}^{-1}$, the highest to date in the phononic gigahertz range. We also find indications that geometric disorder poses a significant challenge towards nanoscale phonon-based technologies.

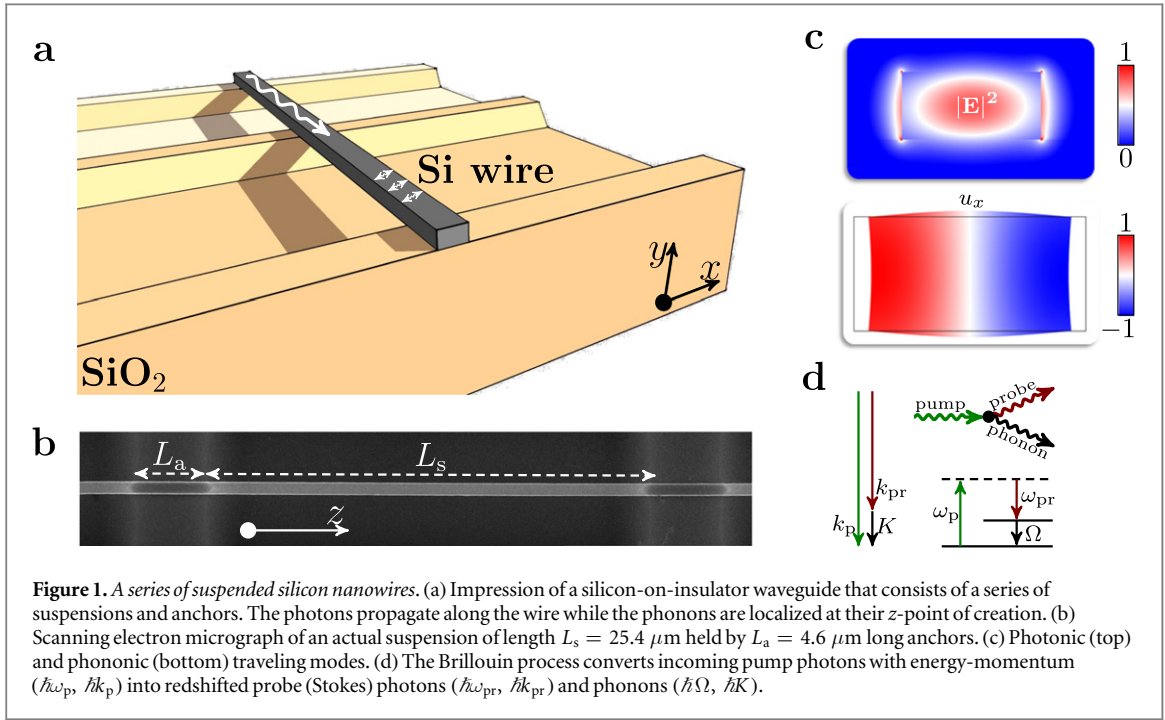
1. Introduction

The interaction between photons and acoustic phonons has been investigated in bulk materials since the 1920s [1, 2]. In case the phonons are generated by optical forces, such as radiation pressure and electrostriction [3–7], the interaction is often called stimulated Brillouin scattering (SBS)—a feedback loop in which energy flows from the optical waves to the mechanical oscillator. Its signature is the narrowband amplification of an optical probe that is red-detuned by the phonon resonance frequency from a strong optical pump.

Although the mechanical linewidth does not exceed 100 MHz typically, there is no such inherent optical bandwidth restriction in SBS: the pump wavelength can be freely tuned in a wide span ($\sim 100 \text{ nm}$) and multiple pumps can be combined to tailor the SBS response [8]. Compared to cavity-based optomechanics [9–15], such a circuit-oriented approach—exploiting wideband waveguides—is intrinsically less power-efficient as the optical field is not resonantly enhanced. Nevertheless, the removal of the optical bandwidth restriction and the accompanying versatility has motivated a great deal of SBS work in small-core waveguides, from photonic crystal [16–18], dual-web [19] and subwavelength [20] fibres to chalcogenide [21–24] and silicon waveguides [3, 4, 25]. It may provide new integrated signal processing capabilities such as tunable RF notch filters [25, 26] and true time delays [27]. The prospect is especially appealing in silicon photonic wires, whose strong confinement enhances the light–matter coupling. Mass-manufacturable silicon-on-insulator chips are therefore an exciting platform for high-density optomechanical circuitry, perhaps even at the quantum level [28–30].

Recent work on this front has demonstrated promising photon–phonon coupling efficiencies in all-silicon waveguides [4]. The coupling was sufficiently strong to bring the waveguides into transparency (i.e. on/off gain equal to the propagation loss), but phonon leakage and free-carrier (FC) absorption precluded actual amplification above the optical propagation loss. Here, we eliminate the phonon clamping loss—observing an increase of the phonon quality factor from 300 up to 1000 at room temperature—by fully suspending the silicon nanowires. Thus, we achieve a modest amount of gain exceeding the optical losses. The waveguides consist of a series of suspended beams, supported by silicon dioxide anchors (figure 1).

Finally, we observed a strong dependence of the phonon quality factor on the number of and distance between the suspensions. This indicates the presence of geometric disorder that broadens and splits the phonon dispersion relation in some cases, similar to Doppler broadening in gas lasers [31]. From a wider perspective and



not limited to our system, such geometric disorder may hinder development of nanoscale phonon circuits quite generally [28–30, 32].

2. Results and discussion

2.1. Theoretical background

The following discussion is concerned with forward intra-modal scattering, in which co-propagating pump and probe waves generate low-wavevector, low-group-velocity acoustic phonons (figure 1(d)).

2.1.1. Brillouin gain

First, we briefly treat the small-signal Brillouin gain in a waveguide consisting of suspensions of length L_s and anchors of length L_a . The section length is $L_{\text{sec}} = L_s + L_a$ and there are $N = \frac{L}{L_{\text{sec}}}$ such sections with L the total waveguide length (figure 1). We denote the input pump power P_p and the red-detuned probe (Stokes) power P_{pr} . As previously shown [4], the power P_{pr} of the probe obeys

$$\begin{aligned} \frac{dP_{pr}}{dz} &= - \left(\tilde{\mathcal{G}} P_p e^{-\alpha z} \mathcal{L} + \alpha \right) P_{pr} \quad \text{suspensions} \\ \frac{dP_{pr}}{dz} &= - \alpha P_{pr} \quad \text{anchors} \end{aligned} \quad (1)$$

in the low-cascading regime and with $\tilde{\mathcal{G}}$ the Brillouin gain coefficient, $\mathcal{L}(\Delta) = \frac{1}{-2\Delta + i}$ the complex Lorentzian, $\Delta = \frac{\Omega - \Omega_m}{\Gamma_m}$ the normalized detuning, Γ_m the phonon linewidth and $\mathcal{L} = -\frac{1}{4\Delta^2 + 1}$. To derive (1), we assumed that the phonon propagation loss far exceeds the photon propagation loss and that the photon–phonon coupling is weak relative to the spatial phonon decay [33]. In particular, in this work the photon decay length α^{-1} is about a centimeter, while the phonons spatially decay over a couple of nanometers in the z -direction [4]. Indeed, the flat dispersion of these Raman-like [5, 17] phonons yields an exceedingly low group velocity [4]. Therefore, each suspension consists of a series of independent mechanical oscillators—whose frequency depends on the local width [4]. This phonon locality also implies that the anchor does not contribute to the Brillouin gain.

We treat the optical loss α as distributed, although it may in fact be partially localized at the interfaces or be unequal in the suspensions and anchors. This is a good approximation as the SBS strength in the next section only depends on the remaining pump power, not on how some of it was lost in the previous sections. The ansatz $P_{pr} = g(z)e^{-\alpha z}$ and piecewise integration of (1) results in

$$\begin{aligned}\ln \frac{g(L)}{g(0)} &= -\tilde{G}P_p L_{s,\text{eff}} \mathcal{JL} \sum_{k=0}^{N-1} e^{-\alpha k L_{\text{sec}}} \\ &= -\tilde{G}P_p L_{s,\text{eff}} \mathcal{JL} \frac{1 - e^{-\alpha L}}{1 - e^{-\alpha L_{\text{sec}}}} \approx -\tilde{G}P_p f_s L_{\text{eff}} \mathcal{JL}\end{aligned}$$

with the effective suspension length $L_{s,\text{eff}} = \frac{1 - e^{-\alpha L}}{\alpha} \approx L_s$ since the sections are much smaller than the optical decay length ($L_{\text{sec}} \ll \alpha^{-1}$) and $f_s = \frac{L_s}{L_{\text{sec}}}$. Therefore we obtain

$$\ln \frac{P_{\text{pr}}(L)}{P_{\text{pr}}(0)e^{-\alpha L}} = \frac{\tilde{G}P_p f_s L_{\text{eff}}}{4\Delta^2 + 1}. \quad (2)$$

These experiments are the circuit analog of cavity-based optomechanically induced transparency [34, 35]. However, our system features spatially stronger mechanical than optical damping, such that it is the optical response that is modified here [33].

2.1.2. Cross-phase modulation

Gain measurements provide access to all relevant optomechanical parameters, but require careful calibration of the on-chip pump power P_p . In contrast, a cross-phase modulation (XPM) measurement [3, 4] is, in absence of FCs, intrinsically calibrated: it provides access to the ratio of the photon–phonon coupling and the electronic Kerr effect independent of pump power. These experiments are the circuit analog of cavity-based coherent wavelength conversion [36], although the conversion need not take place between two optical resonances in our case.

We assume weak XPM and denote the envelopes of the pump and its red- and blue-detuned sidebands a_p , a_{p-} and a_{p+} and similarly for the injected probe a_{pr} and the XPM-imprinted blue-shifted sideband $a_{\text{pr}+}$. The imprinted sideband grows as [4]

$$\begin{aligned}\frac{da_{\text{pr}+}}{dz} &= -\frac{i}{2}(4\gamma_{\text{Ks}} + \tilde{G}\mathcal{L})(a_p a_{p-}^* + a_{p+} a_p^*) a_{\text{pr}} - \frac{\alpha}{2} a_{\text{pr}+} \quad \text{suspensions} \\ \frac{da_{\text{pr}+}}{dz} &= -i2\gamma_{\text{Ka}}(a_p a_{p-}^* + a_{p+} a_p^*) a_{\text{pr}} - \frac{\alpha}{2} a_{\text{pr}+} \quad \text{anchors}\end{aligned}$$

with γ_{K} the Kerr parameter. Note that the XPM can also be seen as a four-wave mixing process with photon creations (a^*) and annihilations (a) given by $a_{\text{pr}+}^*(a_p a_{p-}^* + a_{p+} a_p^*) a_{\text{pr}}$. We assume that the pump and probe remain undepleted by the XPM, but include their absorptive decay. Then we get

$$\begin{aligned}\frac{da_{\text{pr}+}}{dz} &= C_s e^{-\frac{3\alpha}{2}z} - \frac{\alpha}{2} a_{\text{pr}+} \quad \text{suspensions} \\ \frac{da_{\text{pr}+}}{dz} &= C_a e^{-\frac{3\alpha}{2}z} - \frac{\alpha}{2} a_{\text{pr}+} \quad \text{anchors}\end{aligned}$$

with $C_s = \frac{1}{2}(4\gamma_{\text{Ks}} + \tilde{G}\mathcal{L})C$, $C_a = 2\gamma_{\text{Ka}}C$ and $C = -i(a_p a_{p-}^* + a_{p+} a_p^*) a_{\text{pr}}|_{z=0}$. Inserting the ansatz $a_{\text{pr}+}(z) = g(z)e^{-\frac{\alpha}{2}z}$ and piecewise integrating ($g(0) = 0$) yields

$$\begin{aligned}g(L) &\approx (C_s L_s + C_a L_a) \sum_{k=0}^{N-1} e^{-\alpha k L_{\text{sec}}} = (C_s L_s + C_a L_a) \\ &\times \frac{1 - e^{-\alpha L}}{1 - e^{-\alpha L_{\text{sec}}}} \approx (C_s f_s + C_a f_a) L_{\text{eff}}\end{aligned}$$

where we used $L_{a,\text{eff}} \approx L_a$, $L_{\text{eff}} = \frac{1 - e^{-\alpha L}}{\alpha}$ and $f_a = 1 - f_s$. Therefore

$$|a_{\text{pr}+}(L)|^2 = 4\bar{\gamma}_{\text{K}}^2 \mathcal{F} |C|^2 L_{\text{tot,eff}}^2 e^{-\alpha L} \propto \mathcal{F}$$

with the averaged Kerr parameter $\bar{\gamma}_{\text{K}} = \gamma_{\text{Ks}} f_s + \gamma_{\text{Ka}} f_a$, the normalized Fano function

$$\mathcal{F}(\Delta) = \left| 1 + f_s \frac{\tilde{G}}{4\bar{\gamma}_{\text{K}}} \mathcal{L}(\Delta) \right|^2 = |1 + r \mathcal{L}(\Delta)|^2 \quad (3)$$

and $r = f_s \frac{\tilde{G}}{4\bar{\gamma}_{\text{K}}}$ the ratio between the mechanically and Kerr-driven XPM.

Including TPA, FC index changes and FC absorption, (3) no longer holds. For instance, in case of TPA the Kerr parameter should be replaced by $\bar{\gamma}_{\text{K}} \rightarrow \bar{\gamma}_{\text{K}} - i\bar{\gamma}_{\text{TPA}}$ and (3) becomes

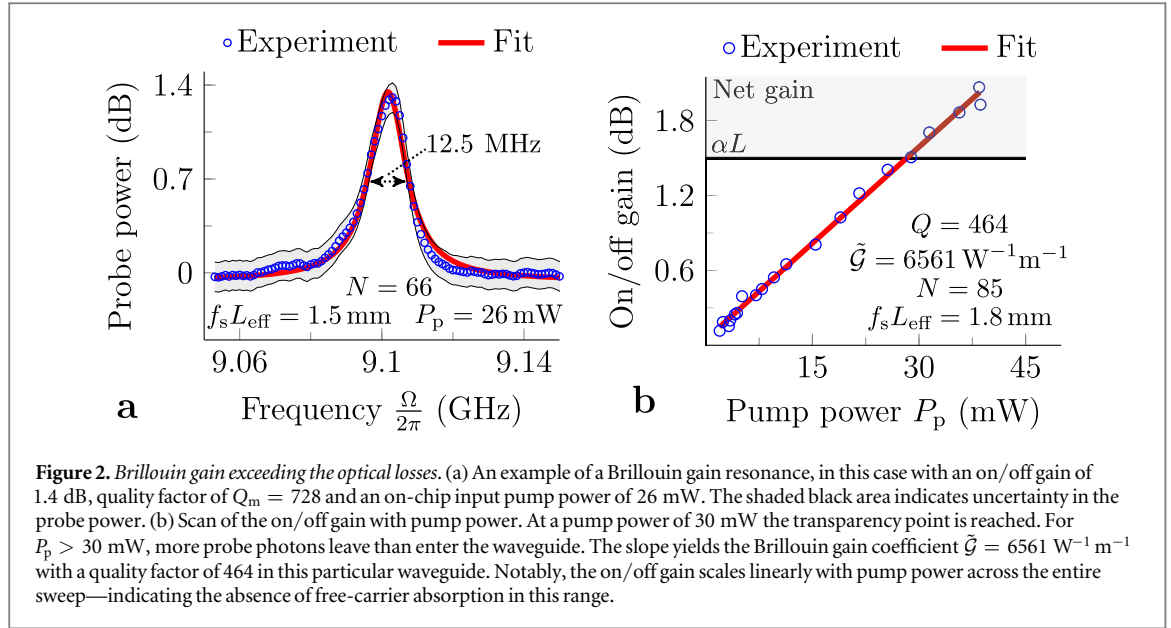


Figure 2. Brillouin gain exceeding the optical losses. (a) An example of a Brillouin gain resonance, in this case with an on/off gain of 1.4 dB, quality factor of $Q_m = 728$ and an on-chip input pump power of 26 mW. The shaded black area indicates uncertainty in the probe power. (b) Scan of the on/off gain with pump power. At a pump power of 30 mW the transparency point is reached. For $P_p > 30$ mW, more probe photons leave than enter the waveguide. The slope yields the Brillouin gain coefficient $\tilde{G} = 6561 \text{ W}^{-1} \text{ m}^{-1}$ with a quality factor of 464 in this particular waveguide. Notably, the on/off gain scales linearly with pump power across the entire sweep—indicating the absence of free-carrier absorption in this range.

$$\mathcal{F}(\Delta) = \left| 1 + e^{i\phi} f_s \frac{\tilde{G}}{4\tilde{\gamma}_{\text{tot}}} \mathcal{L}(\Delta) \right|^2 = \left| 1 + e^{i\phi} r \mathcal{L}(\Delta) \right|^2 \quad (4)$$

with $\tilde{\gamma}_{\text{tot}} = \sqrt{\tilde{\gamma}_K^2 + \tilde{\gamma}_{\text{TPA}}^2}$ and $\tan \phi = \frac{\tilde{\gamma}_{\text{TPA}}}{\tilde{\gamma}_K}$. In our case, the two-photon ϕ is small and positive as $\frac{\tilde{\gamma}_{\text{TPA}}}{\tilde{\gamma}_K} \approx 0.1$. The FC nonlinearity $\tilde{\gamma}_{\text{FC}}$, however, can give rise to negative ϕ (see appendix).

2.2. Fabrication and passive characterization

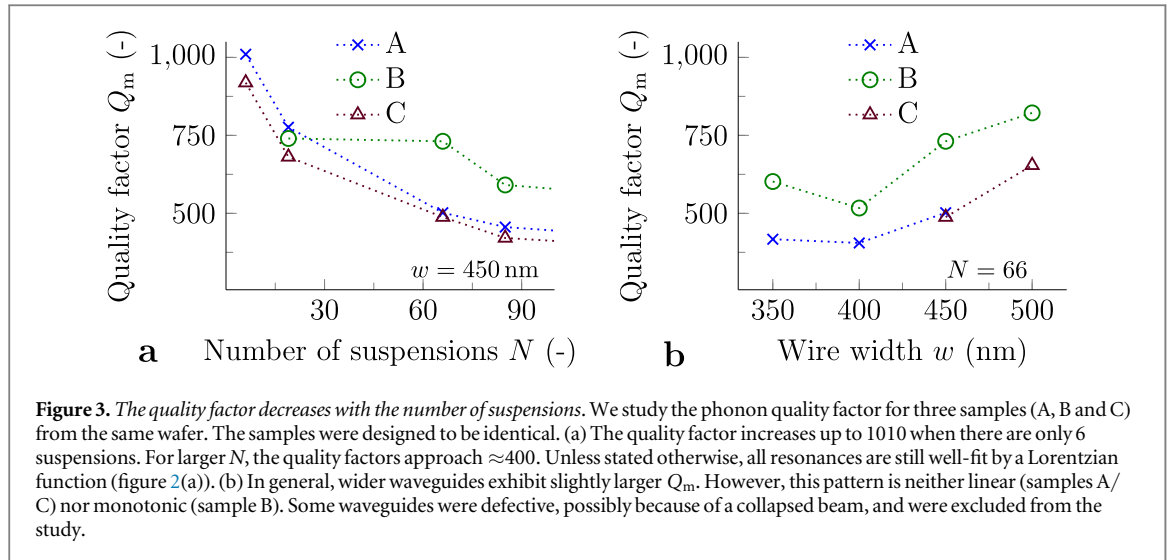
We started from air-cladded 220 nm thick, 450 nm wide silicon-on-insulator wires fabricated by 193 nm UV lithography (www.ePIXfab.eu) at imec. Next, we patterned an array of apertures in a resist spun atop the wires. Then we immersed the chip in buffered hydrofluoric acid, which selectively etches the silicon dioxide substrate, until the wires were released. The end result was a series of suspended beams, each typically 25 μm long and held by 5 μm silicon dioxide anchors (figure 1). Simulations and measurements show that the optical reflections caused by these anchors are negligibly small (see appendix). We found optical losses $\alpha \approx 5.5 \text{ dB cm}^{-1}$ by the cut-back method, which are a factor 2 larger than before the etch. This is likely related to a deterioration of the wires' surface state and consistent with both (1) the measured drop in FC lifetime (see appendix) and (2) the decrease in FC absorption found in the gain experiment (figure 2(b)).

2.3. Optomechanical experiments

In this section, we discuss the guided-wave optomechanical characterization of a series of suspended silicon nanobeams. We used the experimental set-ups presented in [4] and reproduced in the appendix. Our device is characterized by the suspension length L_s , the anchor length L_a , the section length $L_{\text{sec}} = L_s + L_a$, the number of suspensions N , the total length $L = NL_{\text{sec}}$, the total effective length $L_{\text{eff}} = \frac{1 - e^{-\alpha L}}{\alpha}$, the suspended fraction $f_s = \frac{L_s}{L_{\text{sec}}}$ and the waveguide width w . Unless stated otherwise, these parameters have values $L_s = 25.4 \mu\text{m}$, $L_a = 4.6 \mu\text{m}$, $L_{\text{sec}} = 30 \mu\text{m}$, $N = 85$, $L = 2535 \mu\text{m}$, $L_{\text{eff}} = 2168 \mu\text{m}$, $f_s = 0.85$ and $w = 450 \text{ nm}$. In some cases, our waveguides have a non-suspended input/output section before/after the cascade of suspended nanobeams. We take this into account when calculating input pump powers (gain experiment) or suspended fractions (XPM experiment). We focus on this sub-centimeter wire as longer waveguides suffer from a decreased mechanical quality factor (figure 3(a)).

2.3.1. Brillouin gain

First, we measured the amplitude response of our system. We injected a weak probe red-detuned from a strong pump and retrieved the probe power as a function of detuning (figure 2(a)). As before [4], we find gain resonances around 9.1 GHz. The on/off gain increases with pump power (figure 2(b)) and reaches the transparency point $\tilde{G}P_p = \alpha$ around $P_p = 30$ mW. Beyond this pump power, the output exceeds the input probe photon flux. At the maximum pump power of 39 mW, we obtain guided-wave cooperativities [33] of $\tilde{C} = \frac{(f_s \tilde{G}) P_p}{\alpha} = 1.7$. This modest net gain of 0.5 dB (figure 2(b)) is a step towards selective on-chip amplifiers that



could be used for homodyne detection, in order to eliminate the requirement of a phase-stabilized local oscillator [37].

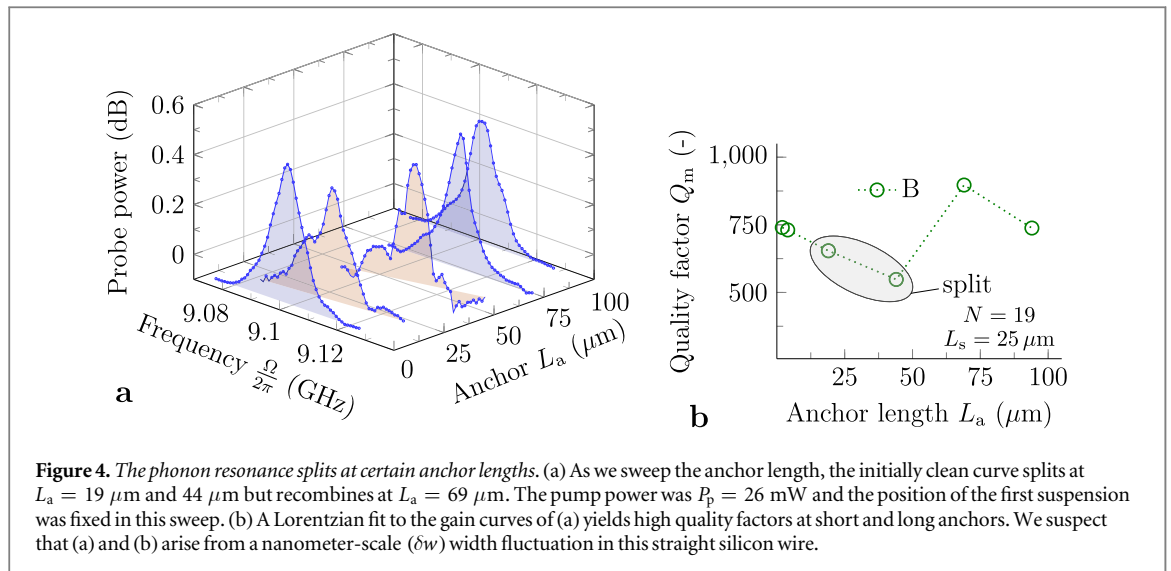
Notably, the linear scaling between on/off gain and pump power (figure 2(b)) indicates the absence of FC absorption up to 40 mW [38, 39]. In contrast, we previously measured increased nonlinear absorption already at 25 mW in silicon wires on a pillar [4]. Both this finding and the higher propagation losses (5.5 dB cm^{-1} instead of 2.6 dB cm^{-1} [4]) likely originate in a deterioration of the wires' surface state during the fabrication of the suspensions. In agreement with this hypothesis, we measured a drop in the FC lifetime (see appendix).

In case this structure were to be placed in a cavity, such as a silicon microring, it would also have to overcome coupling losses to achieve the photon/phonon lasing threshold ($\tilde{\mathcal{C}} > \mathcal{C} = 1$ [33]). We note that the acoustic linewidth (~ 10 MHz) is a factor 10^2 smaller than typical optical linewidths of silicon microcavities (~ 1 GHz). Therefore, this would produce stimulated emission of phonons, not photons [12, 15, 33, 40–42]. Such a device would not benefit from the spectral purification associated with Brillouin lasers [43, 44]. The origin of this reversal of the damping hierarchy (going from waveguides to cavities) [33, 42] lies in the exceedingly low group velocity of these Raman-like [17] acoustic phonons; indeed, despite enormously higher propagation losses they usually still have lower linewidths than photons [12, 33, 42]. Only uniquely high-quality optical cavities, to date realized only using silica [23, 45–48] or crystalline [10] materials, can produce lower photonic than phononic damping rates.

2.3.2. Geometric disorder

Next, we study the quality factor extracted from the gain resonances (figure 2(a)). We find that it strongly decreases with the number of suspensions N (figure 3(a)); from $Q_m \approx 10^3$ at $N = 6$ to $Q_m \approx 400$ at $N = 85$. For larger numbers of suspensions in a spiral configuration ($N = 1332$, not shown), the quality factor levels off around $Q_m \approx 340$. Notably, this relation changes from sample to sample—even if they originate from the same wafer (figure 3(a)). We attribute such variations to inhomogeneous broadening by geometric disorder, presumably in the width of the nanowires [4]. Indeed, the sensitivity of the resonance frequency $\frac{\Omega_m}{2\pi}$ to width variations is $\frac{1}{2\pi} \frac{d\Omega_m}{dw} \approx 20 \text{ MHz nm}^{-1}$ [4]. Therefore, realistic width variations δw of about 0.5 nm [49, 50] yield inhomogeneous linewidths of about $\frac{\Gamma_{\text{inh}}}{2\pi} \approx 10 \text{ MHz}$ —comparable to those measured (figure 2(a)). Similar disorder has been studied in snowflake crystals [29].

Further, we investigated the influence of the width w on the quality factor Q_m . Since the resonance frequency scales inversely with width ($\frac{\Omega_m}{2\pi} \propto w^{-1}$) [4], its sensitivity scales inverse quadratically with width ($\frac{d\Omega_m}{dw} \propto w^{-2}$). Subsequently, the inhomogeneously broadened linewidth scales similarly ($\Gamma_{\text{inh}} \propto w^{-2}$) in case the size of the width variations δw does not depend on w . Then the quality factor scales linearly with width ($Q_m = \frac{\Omega_m}{\Gamma_m} \propto w$). We indeed observe overall larger quality factors for wider wires, although this pattern is neither linear nor monotonic (figure 3(b)). We note that, unless stated otherwise, all resonances were still well-fit by a Lorentzian function (figure 2(a)). In case of sufficiently sampled geometric disorder, the gain curves would become convolutions of a Lorentzian and a probability function describing the geometric disorder (e.g. distribution of the width w). The largest deviations of such Voigt curves with respect to a Lorentzian occur in the tails (large $\Delta = \frac{\Omega - \Omega_m}{\Gamma_m}$), precisely where the relative uncertainty in the measured probe power is highest (figure 2(a)). Given this uncertainty, both Lorentzian and e.g. Gaussian-shaped curves produce good fits to the gain resonances. A



low-temperature characterization would yield more information regarding the nature of the acoustic broadening mechanisms.

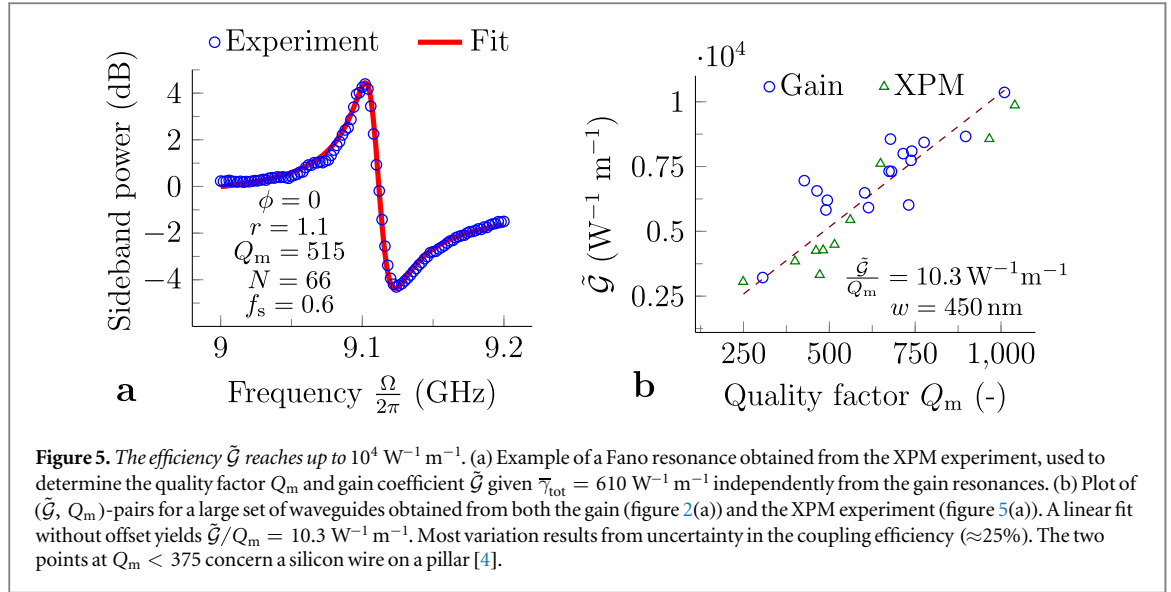
There are two types of potential width fluctuations: (1) fast sidewall roughness with a small coherence length L_{coh} (on the order of 50 nm [51]) and (2) slow variations in the average waveguide width w with a much larger coherence length (on the order of $100 \mu\text{m}$). We suspect that mechanism (2) is at play here, since even an individual section ($L_{\text{sec}} \approx 30 \mu\text{m}$) is much larger than the coherence length ($\approx 50 \text{ nm}$ [51]) of the surface roughness. Therefore, sidewall roughness cannot explain the significant changes of Q_m with N (figure 3(a)): even a single section samples it fully ($L_{\text{sec}}/L_{\text{coh}} \approx 600$). In contrast, slow excursions of the waveguide width are consistent with such behavior. We confirm this by scanning the anchor length L_a while keeping the number of suspensions N and the suspension length L_s constant (figure 4). In this sweep, the position of the first suspension is fixed. As L_a increases, the initially clean resonance first splits at $L_a = 19 \mu\text{m}$ and then recombines at $L_a = 69 \mu\text{m}$ (figure 4(a)). Remarkably, the $L_a = 69 \mu\text{m}$ wire even produces the highest quality factor (figure 4(b)). In light of the above discussion, this behavior likely stems from a nanometer-scale (δw) width excursion: short and long anchor waveguides avoid the width fluctuations and thus yield clean profiles. Both figures 3 and 4 are fingerprints of geometric disorder that hinders the development of integrated Brillouin-based technologies.

2.3.3. Photon-phonon overlap

Finally, we measure the XPM resonances (figure 5(a)) for a subset of waveguides to obtain an independent estimate of the photon–phonon interaction efficiency. Combined with the gain data, we obtain the (\tilde{G}, Q_m) -pairs for a large set of waveguides (figure 5(b)) with fixed waveguide width $w = 450 \text{ nm}$. A fit (figure 5(b)) to this dataset yields a non-resonant nonlinearity of $\frac{\tilde{G}}{Q_m} = 10.3 \text{ W}^{-1} \text{ m}^{-1}$ —in good agreement with earlier experiments [4] and predictions [5, 6]. The efficiencies reach up to $\tilde{G} = 10360 \text{ W}^{-1} \text{ m}^{-1}$, the highest value obtained thus far in the gigahertz range. Flexible megahertz-class systems in vacuum can produce up to $\tilde{G} = 10^6 \text{ W}^{-1} \text{ m}^{-1}$ at 6 MHz [19]. Previous gigahertz systems achieved $\tilde{G} = 3100 \text{ W}^{-1} \text{ m}^{-1}$ in silicon pedestal waveguides at 9.2 GHz [4], $\tilde{G} = 2328 \text{ W}^{-1} \text{ m}^{-1}$ in hybrid silicon/silicon nitride waveguides at 1.3 GHz [3] and $\tilde{G} = 304 \text{ W}^{-1} \text{ m}^{-1}$ in chalcogenide rib waveguides at 7.7 GHz [52].

3. Conclusion

Through a novel opto-acoustic nanodevice, a series of suspended silicon wires, we demonstrate modest (0.5 dB) net Brillouin gain with high efficiencies (up to $10^4 \text{ W}^{-1} \text{ m}^{-1}$). This device is a step towards integrated selective amplifiers. We find that fabrication disorder, likely in the waveguide width, broadens and splits the phonon resonances in some cases. In particular, the phonon quality factor strongly decreases as the number of suspended silicon beams increases. Such disorder is expected to hinder development of nanoscale phonon-based technologies quite generally—new techniques or better fabrication tools must be developed to address this issue.



Acknowledgments

RVL acknowledges the Agency for Innovation by Science and Technology in Flanders (IWT) for a PhD grant and AB the ITN-network cQOM for a postdoc grant. This work was partially funded under the FP7-ERC-InSpectra programme.

Appendix

A.1. Influence of TPA and FCs on XPM

In this section, we describe the influence of TPA and FCs on the Fano resonances. First, we recall that (see (3)), in absence of TPA and FCs, the sideband power is proportional to \mathcal{F} with

$$\mathcal{F}(\Delta) = \left| 1 + r \frac{1}{-2\Delta + i} \right|^2 \quad (5)$$

with $r = f_s \frac{\tilde{\mathcal{G}}}{4\bar{\gamma}_K}$. One can show that this Fano function \mathcal{F} has one maximum \mathcal{F}_{max} and one minimum \mathcal{F}_{min} given by

$$\mathcal{F}_{\text{max}} = \frac{r^2 + 4 + r\sqrt{r^2 + 4}}{r^2 + 4 - r\sqrt{r^2 + 4}} = \frac{1}{\mathcal{F}_{\text{min}}} \quad (6)$$

that are fully determined by r . This implies $\mathcal{F}_{\text{max}}[\text{dB}] = -\mathcal{F}_{\text{min}}[\text{dB}]$, as evident in figure 5(a). Inverting this for r yields

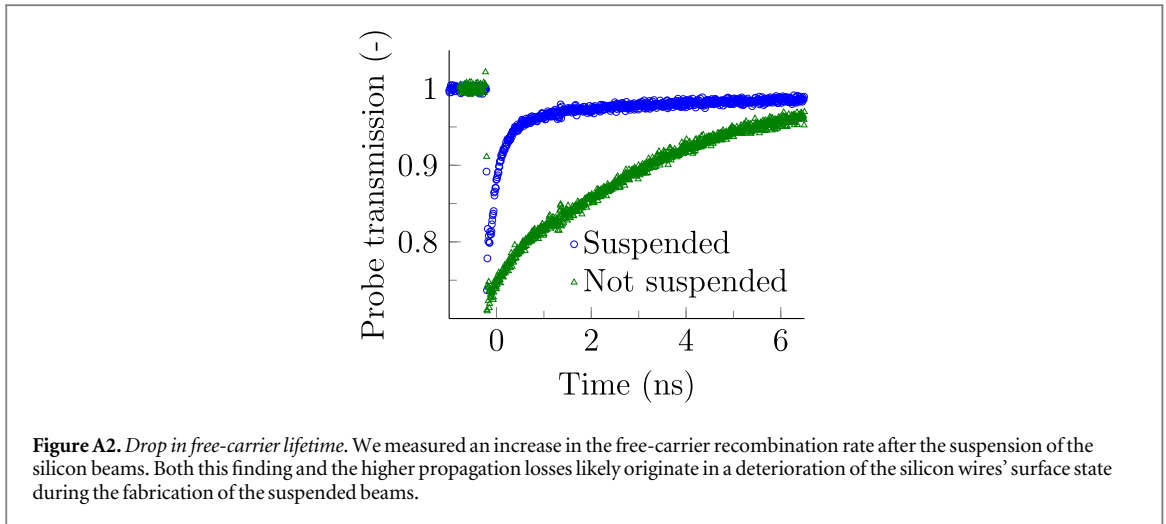
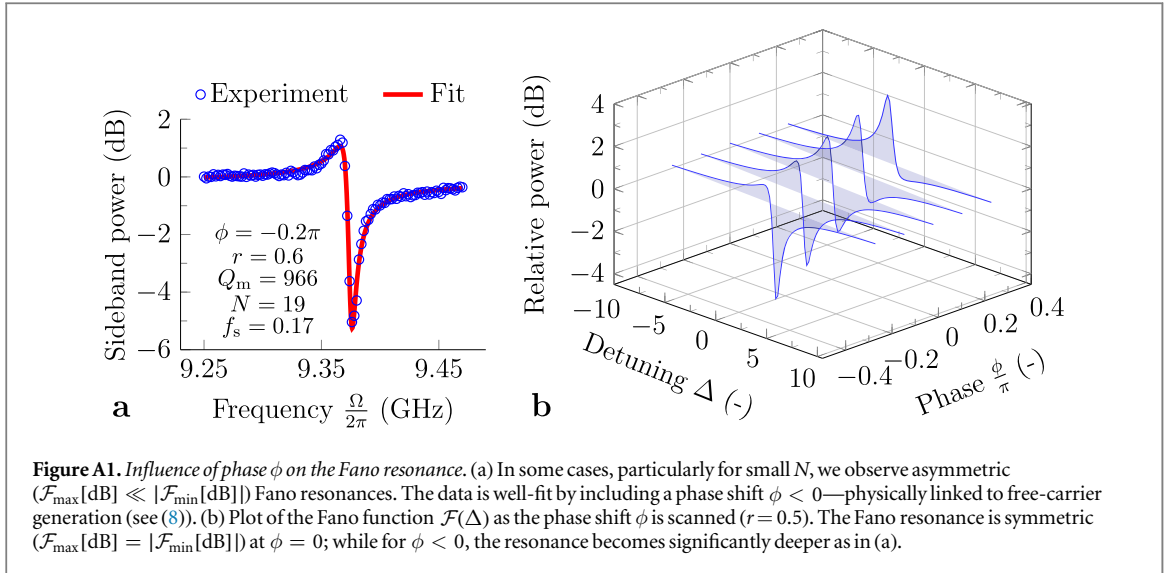
$$r = \frac{\mathcal{F}_{\text{max}} - 1}{\sqrt{\mathcal{F}_{\text{max}}}}. \quad (7)$$

Applied to figure 5(a), we have $\mathcal{F}_{\text{max}} = 4.4 \text{ dB} = 2.75$ and thus $r = 1.1$ through (7)—in agreement with the r obtained from a least-square fit (figure 5(a)). The extrema are reached at a detuning of $\Delta_{\text{max/min}} = \frac{1}{4} \left(r \mp \sqrt{r^2 + 4} \right)$. In the large r limit, we get $\Delta_{\text{max}} \rightarrow -\frac{1}{2r}$ and $\Delta_{\text{min}} \rightarrow \frac{r}{2}$. In the small r limit, we have $\Delta_{\text{max/min}} \rightarrow \frac{r \mp 2}{4}$. Therefore, the maximum XPM is always reached at a negative detuning between $-\frac{1}{2}$ and 0, typically ($r > 1$) close to the phonon resonance ($\Delta = 0$).

In some cases, we observe $\mathcal{F}_{\text{max}}[\text{dB}] \ll |\mathcal{F}_{\text{min}}[\text{dB}]|$ —a clear indication that (5) is too simplistic. It turns out that the Fano function (5) must be replaced by [3]

$$\mathcal{F}(\Delta) = \left| 1 + e^{i\phi} r \frac{1}{-2\Delta + i} \right|^2 \quad (8)$$

with $r = f_s \frac{\tilde{\mathcal{G}}}{4\bar{\gamma}_{\text{tot}}}$ and $\bar{\gamma}_{\text{tot}} = |\bar{\gamma}_K - i\bar{\gamma}_{\text{TPA}} + \bar{\gamma}_{\text{FC}}\bar{P}|$ the total nonlinearity, including TPA and FC effects, $\phi = -\angle(\bar{\gamma}_K - i\bar{\gamma}_{\text{TPA}} + \bar{\gamma}_{\text{FC}}\bar{P})$ and \bar{P} the average power in the waveguide. The FC nonlinearity $\bar{\gamma}_{\text{FC}}$ is complex as free carriers modulate both the index and the absorption—both effects create an imprinted sideband on the probe; in addition, $\bar{\gamma}_{\text{FC}}(\Omega)$ depends on the modulation frequency since free carriers do not respond



instantaneously. This is a slow dependency, so we take $\bar{\tau}_{\text{FC}}$ constant in the range of our sweep [3]. This can be shown by solving for the carrier dynamics [53]

$$\partial_t N_c = \frac{\beta_{\text{TPA}}}{2\hbar\omega} P^2 - \kappa_c N_c \quad (9)$$

in frequency-domain and using the proportionality $\Delta n \propto -N_c$ and $\Delta\alpha \propto N_c$ between both the index and absorption and the carrier concentration [53]. Here we denote β_{TPA} the TPA coefficient and κ_c the FC recombination rate.

Notably, $\phi > 0$ in absence of free carriers ($\bar{\tau}_{\text{FC}} = 0$). The observed $\phi < 0$ (figure A1 (a)) is thus linked to the presence of free carriers; in addition, we still use $\bar{\tau}_{\text{tot}} \approx \bar{\tau}_{\text{K}} \approx 610 \text{ W}^{-1} \text{ m}^{-1}$ on the assumption that the Kerr effect remains the dominant background nonlinearity. This is consistent with the observations that (1) in most cases $\mathcal{F}_{\max}[\text{dB}] \approx -\mathcal{F}_{\min}[\text{dB}]$ and thus $\phi \approx 0$, (2) the background is flat (figures 5 and A1(a)) and (3) the Brillouin efficiencies deduced from the XPM experiment are in reasonable agreement with those inferred from the gain experiment (figure 5(b)).

A.2. Drop in FC lifetime

Using the set-up presented in [4], we measured a significant drop in the FC lifetime (figure A2) in the suspended beams with respect to the regular non-suspended waveguide. Both this finding and the higher propagation losses likely originate in a deterioration of the silicon wires' surface state during the fabrication of the suspended beams.

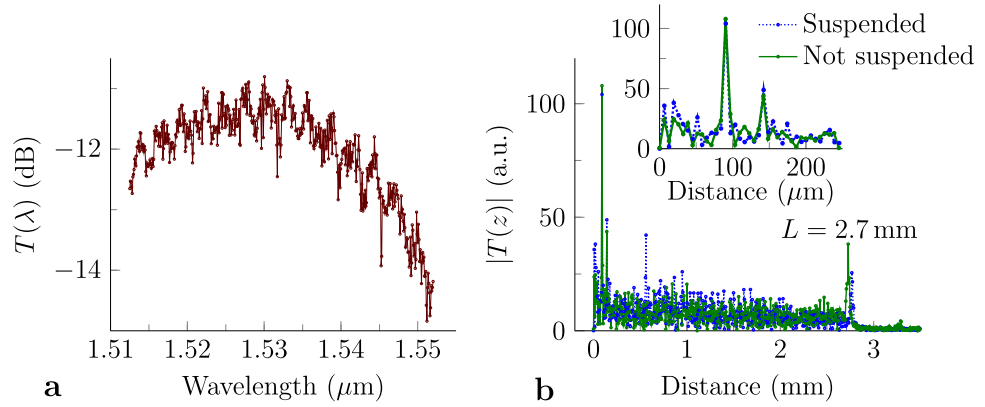


Figure A3. The interface reflections are small. (a) The fiber-to-fiber transmission spectrum shows the grating bandwidth. It exhibits a slight (1 dB) variation at a free spectral range of about 2.9 nm, both in standard and suspended silicon-on-insulator waveguides. (b) The Fourier transform of this spectrum reveals potential cavities present in the wire. We compare the regular wire (green) to a wire with 85 suspensions ($L_s = 25.4 \mu\text{m}$) and anchors ($L_a = 4.6 \mu\text{m}$) (blue). The distance-axis was calibrated with a group index of $n_g = 4.7$ and shows the waveguide length of 2.7 mm because of grating coupler reflections. These are weaker in the suspended case owing to the higher propagation loss. The 2.9 nm free spectral range (a) shows up at $90 \mu\text{m}$ ((b), inset). Generally, the two Fourier spectra are nearly identical and do not exhibit notable peaks related to the suspension.

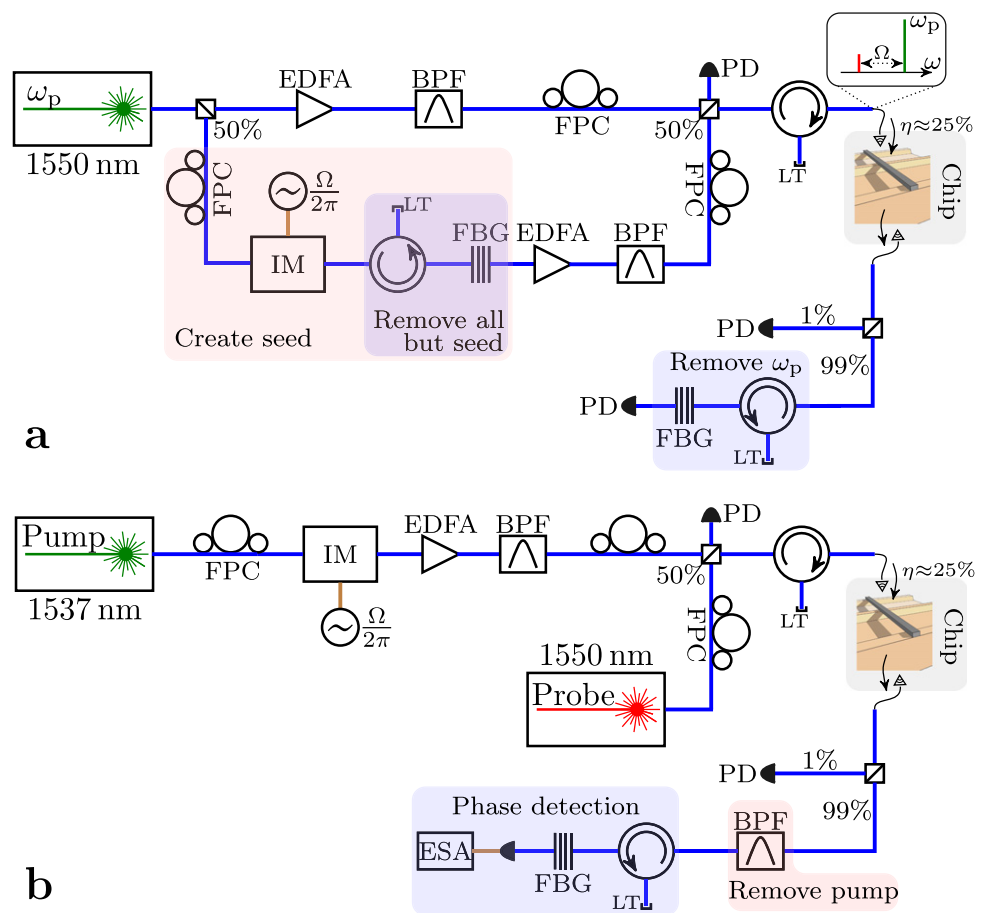


Figure A4. Measurement apparatus used to measure the Brillouin gain profiles (figure 2(a)) by scanning the red-detuning $\frac{\Omega}{2\pi}$ of a probe with respect to a fixed pump wave (a) and to retrieve the Fano-like four-wave mixing resonances (figure 5(a)) by scanning the XPM frequency $\frac{\Omega}{2\pi}$ (b). The abbreviations are erbium-doped fiber amplifier (EDFA), fiber polarization controller (FPC), intensity modulator (IM), bandpass filter (BPF), light trap (LT), photodetector (PD), fiber Bragg grating (FBG) and electrical spectrum analyzer (ESA).

A.3. The interface reflections are negligible

Our device has discontinuities between the suspended nanobeams and the beams fixed at the anchors (figure 1). Since the beams are spaced periodically, optical reflections may build up. However, we simulated an upper bound for the Fresnel reflection at the discontinuity of less than 10^{-4} —indicating that reflections are negligibly small. Empirically, there are indeed no notable differences in the transmission spectrum of a regular waveguide versus that of a suspended waveguide (figure A3). Therefore, our device can be treated as a single-pass structure.

A.4. The measurement set-ups

The measurement set-ups for the gain and XPM experiment were identical to those presented in [4]. They are depicted in figure A4 for completeness.

References

- [1] Boyd R 2008 *Nonlinear Optics* 3rd edn (London: Elsevier)
- [2] Agrawal G 2013 *Nonlinear Fiber Optics* 5th edn (New York: Academic)
- [3] Shin H, Qiu W, Jarecki R, Cox J, Olsson R, Starbuck A, Wang Z and Rakich P 2013 *Nat. Commun.* **4** 1944
- [4] Van Laer R, Kuyken B, Van Thourhout D and Baets R 2015 *Nat. Photonics* **9** 199–203
- [5] Rakich P, Reinke C, Camacho R, Davids P and Wang Z 2012 *Phys. Rev. X* **2** 1–5
- [6] Qiu W, Rakich P T, Shin H, Dong H, Soljačić M and Wang Z 2013 *Opt. Express* **21** 31402
- [7] Wolff C, Steel M J, Eggleton B J and Poulton C G 2015 *Phys. Rev. A* **92** 013836
- [8] Thévenaz L 2008 *Nat. Photonics* **2** 447–509
- [9] Carmon T, Rokhsari H, Yang L, Kippenberg T and Vahala K 2005 *Phys. Rev. Lett.* **94** 223902
- [10] Grudinin I, Matsko A and Maleki L 2009 *Phys. Rev. Lett.* **102** 043902
- [11] Tomes M and Carmon T 2009 *Phys. Rev. Lett.* **102** 113601
- [12] Aspelmeyer M, Kippenberg T and Marquardt F 2014 *Rev. Mod. Phys.* **86** 1391–452
- [13] Chan J, Alegre T, Safavi-Naeini A, Hill J, Krause A, Gröblacher S, Aspelmeyer M and Painter O 2011 *Nature* **478** 89–92
- [14] Bahl G, Tomes M, Marquardt F and Carmon T 2012 *Nat. Phys.* **8** 203–7
- [15] Cohen JD, Meenehan SM, MacCabe G S, Gröblacher S, Safavi-Naeini A H, Marsili F, Shaw M D and Painter O 2015 *Nature* **520** 522–5
- [16] Dainese P, Russell P S J, Joly N, Knight J C, Wiederhecker G S, Fragnito H L, Laude V and Khelifa 2006 *Nat. Phys.* **2** 388–92
- [17] Kang M, Nazarkin A, Brenn A and Russell P 2009 *Nat. Phys.* **5** 276–80
- [18] Kang M, Butsch A and Russell P 2011 *Nat. Photonics* **5** 549–53
- [19] Butsch A, Koehler J, Noskov R and Russell P 2014 *Optica* **1** 158–64
- [20] Beugnot J C, Lebrun S, Pauliat G, Maillotte H, Laude V and Sylvestre T 2014 *Nat. Commun.* **5** 5242
- [21] Pant R, Poulton C G, Choi D Y, Mcfarlane H, Hile S, Li E, Thevenaz L, Luther-Davies B, Madden S J and Eggleton B J 2011 *Opt. Express* **19** 8285–90
- [22] Eggleton B, Poulton C and Pant R 2013 *Adv. Opt. Photonics* **5** 536–87
- [23] Kabakova I 2013 *Opt. Lett.* **38** 3208–11
- [24] Marpaung D, Morrison B, Pagani M, Pant R, Choi D, Davies B, Madden S and Eggleton B 2015 *Optica* **2** 76–83
- [25] Shin H, Cox J a, Jarecki R, Starbuck A, Wang Z and Rakich P T 2015 *Nat. Commun.* **6** 6427
- [26] Casas-bedoya A, Morrison B, Pagani M, Marpaung D and Eggleton B J 2015 *Opt. Lett.* **40** 4154–7
- [27] Zhu Z, Gauthier D and Boyd R 2007 *Science* **318** 1748–50
- [28] Habraken S J M, Stannigel K, Lukin M D, Zoller P and Rabl P 2012 *New J. Phys.* **14** 115004
- [29] Safavi-Naeini A H, Hill J T, Meenehan S, Chan J, Gröblacher S and Painter O 2014 *Phys. Rev. Lett.* **112** 153603
- [30] Safavi-Naeini A H and Painter O 2011 *New J. Phys.* **13** 013017
- [31] Saleh B and Teich M 1991 *Fundamentals of Photonics* (New York: Wiley)
- [32] Hatanaka D, Mahboob I, Onomitsu K and Yamaguchi H 2014 *Nat. Nanotechnology* **9** 520–4
- [33] Van Laer R, Baets R and Van Thourhout D 2015 arXiv:1503.03044
- [34] Weis S, Rivière R, Deléglise S, Gavartin E, Arcizet O, Schliesser A and Kippenberg T 2010 *Science* **330** 1520–3
- [35] Safavi-Naeini A H, Mayer Alegre T P, Chan J, Eichenfield M, Winger M, Lin Q, Hill J T, Chang D E and Painter O 2011 *Nature* **472** 69–73
- [36] Hill J T, Safavi-Naeini A H, Chan J and Painter O 2012 *Nat. Commun.* **3** 1196
- [37] Atkins C, Cotter D, Smith D and Wyatt R 1986 *Electron. Lett.* **22** 556–8
- [38] Wolff C, Gutsche P, Steel M J, Eggleton B J and Poulton C G 2015 arXiv:1508.02458
- [39] Wolff C, Gutsche P, Steel M J, Eggleton B J and Poulton C G 2015 *J. Opt. Soc. Am. B* **32** 1968–78
- [40] Grudinin I, Lee H, Painter O and Vahala K 2010 *Phys. Rev. Lett.* **104** 083901
- [41] Shen Y and Bloembergen N 1965 *Phys. Rev.* **290** A1787
- [42] Nunnenkamp A, Sudhir V, Feofanov A, Roulet A and Kippenberg T 2014 *Phys. Rev. Lett.* **113** 023604
- [43] Debut A, Randoux S and Zemmouri J 2000 *Phys. Rev. A* **62** 023803
- [44] Debut A, Stéphane R and Jaouad Z 2001 *J. Opt. Soc. Am.* **18** 556–67
- [45] Lee H, Chen T, Li J, Yang K Y, Jeon S, Painter O and Vahala K J 2012 *Nat. Photonics* **6** 369–73
- [46] Li J, Lee H and Vahala K 2014 *Opt. Lett.* **39** 287–90
- [47] Stokes L F, Chodorow M and Shaw H J 1982 *Opt. Lett.* **7** 509–11
- [48] Li J, Lee H, Chen T and Vahala K J 2012 *Opt. Express* **20** 369–73
- [49] Selvaraja S, Bogaerts W, Dumon P, Van Thourhout D and Baets R 2010 *IEEE J. Sel. Top. Quantum Electron.* **16** 316–24
- [50] Selvaraja S, De Heyn P, Winroth G, Ong P, Lepage G, Cailler C and Absil P 2014 *OSA Technical Digest (OFC Conf.) Th2A.33*
- [51] Lee K K, Lim D R, Luan H C, Agarwal A, Foresi J and Kimerling L C 2000 *Appl. Phys. Lett.* **77** 1617
- [52] Pant R, Marpaung D, Kabakova I V, Morrison B, Poulton C G and Eggleton B J 2014 *Laser Photonics Rev.* **8** 653–66
- [53] Dekker R, Usechak N, Först M and Driessen a 2007 *J. Phys. D: Appl. Phys.* **40** 249–71